OPEN ACCESS
IOP Publishing
Journal of Micromechanics and Microengineering
J. Micromech. Microeng. **35** (2025) 025003 (16pp)
https://doi.org/10.1088/1361-6439/ada165

Residual stress chevron preloading amplifier for large-stroke stiffness reduction of silicon flexure mechanisms

Loïc Tissot-Daguette[1,*], Florent Cosandier[1], Quentin Gubler[1], Yves Pétremand[2], Michel Despont[2] and Simon Henein[1]

[1] INSTANT-LAB—IGM—STI—EPFL (École Polytechnique Fédérale de Lausanne), Neuchâtel, Switzerland
[2] CSEM SA (Centre Suisse d'Électronique et de Microtechnique), Neuchâtel, Switzerland

E-mail: loic.tissot-daguette@epfl.ch

Received 24 September 2024, revised 3 December 2024
Accepted for publication 19 December 2024
Published 9 January 2025

Abstract

Residual stresses can be advantageously used to permanently preload flexure micro-mechanisms in order to modify their deflection and stiffness. This paper presents a new preloading chevron mechanism (PCM) used to amplify the preloading effect of thin film residual stress. To evaluate the preloading performances of this structure, the deflection characteristics of buckled beams and flexure linear stages preloaded by a PCM is investigated experimentally. All the mechanisms are manufactured from a monocrystalline silicon substrate using deep reactive ion etching and residual stress is provided by wet thermal oxidation. Measurements show that the deflection magnitude of fixed-fixed oxidized silicon buckled beams can be increased by up to 5 times when a PCM is integrated. The flexure linear stages studied in this research are composed of a parallel leaf spring stage connected to two fixed-guided buckled beams preloaded by a PCM. Depending on the beam dimensions, the stage translational stiffness can be set to a specific value. We designed a near-zero positive stiffness linear stage revealing a measured stiffness reduction of 98%, and a bistable linear stage with a constant negative stiffness region. Thanks to the elevated preloading displacement supplied by the PCM, the operating stroke (actuation region where the stiffness remains constant) is relatively large (more than 0.4 mm travel for 2.59 mm leaf spring length). The analytical and numerical models carried out to design the mechanisms are in good agreement with the experimental data. The results show that the fixed frame stiffness has a significant effect on the preloading performances due to the substantial forces exerted by the PCM. Furthermore, the presented preloading concept, modeling and sizing method could be applied to other compliant mechanism designs, scales and materials, enabling applications in microelectromechanical systems and watchmaking.

Keywords: residual stress, chevron amplification mechanism, thermal oxidation of silicon, beam buckling, flexure mechanism, bistable mechanism, stiffness reduction

* Author to whom any correspondence should be addressed.

1. Introduction

Residual stress is generally considered as problematic in most applications since the material are prone to unintended breaking, deformation or delamination [1–3]. Nevertheless, residual stress can be highly beneficial to preload or unload compliant micro mechanisms for stiffness tuning [4] or, to generate bistable deflections [5–9]. At macroscale, preloading of compliant mechanisms can be performed using manual translation stages [10–14], loading spacers [15] or actuators [16]. However, in micro-electromechanical systems (MEMS), conventional preloading is usually avoided due to the limitation of space, adjustment precision and the risk of damaging the device. Existing methods to modify the stiffness of MEMS mechanisms include: on/off preloading enabled via external acceleration [17]; the use of inclined or curved beams [18–21]; and electrostatic preloading [22, 23]. On the other hand, residual stress has the advantage of permanently preloading micro-mechanisms, meaning that no energy consumption is required to maintain the preload after fabrication.

Although a variety of thin film coating of a silicon flexure mechanisms can be used for producing a residual stress, thermal oxidation is an appealing option because it produces a compressive stress for spring softening, is highly conformal and can be grown to the desired thickness very accurately. The primary components of this residual stress are intrinsic and thermal stresses [1, 2, 24]. Intrinsic stress is created during the oxidation process due to changes of materials microstructure. Whereas thermal stress is a consequence of the coefficients of thermal expansion mismatch between silicon and silicon dioxide that creates thermal strain during the cooling (from oxidation temperature to room temperature). The effective value of the residual stress can be tuned as it depends on the thermal oxidation process parameters (temperature, including ramping speed, atmosphere and pressure). It is also to note that the measurement methods used to determine the residual stress are indirect which bring some uncertainty. For instance, the residual stress of thermal oxide on silicon can vary from −258 MPa to −331 MPa (compressive stress is conventionally represented by a negative sign) using different measurement methods [3, 25, 26].

Figure 1 illustrates a practical implementation compatible with silicon wafer fabrication of a simple fixed-fixed beam encased in a large cross-section frame, which is more rigid and hence less subject to deformation. A conformal coating producing compressive residual stress (e.g. thermally grown silicon oxide), will tend to extend the beam, reducing its lateral stiffness, and causing it to buckle if the stress is large enough [5, 6]. The same prestressing technique can be applied at the level of flexure-based micro mechanisms to advantageously reduce their stiffness (and the resonance frequency) in some degrees of freedom while keeping the structure stiff in the support directions [6]. Nevertheless, the primary disadvantage of residual stress is its limited preloading strain. For instance, silicon beams prestressed by thermal oxidation have usually a

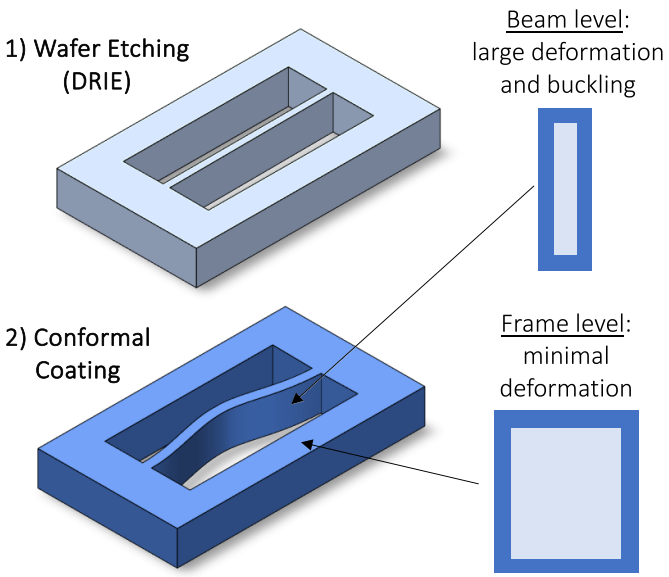

Figure 1. Fixed-fixed beam buckling under the effect of residual stress from conformal coating.

longitudinal strain that does not exceed 0.1% [4, 6]. It results in small buckled beam deflection [6], which leads to minimum stroke for flexure mechanisms [4].

In this paper, we present a new preloading chevron mechanism (PCM) based on a series of beam arranged in a V-shape—chevron architecture—that aims to amplify the effect of the residual stress to efficiently preload micro-scale compliant mechanisms (patent pending [27]). In comparison to existing preloading techniques, the PCM is a building block that offers multiple advantages in reducing the inherent stiffness of flexure-based mechanisms. Indeed, the PCM based on residual stress is compatible with current microfabrication processes, space efficient (see remark 3) and does not require power after fabrication to maintain its preload (permanent preloading). Moreover, the stiffness can be reduced in specific degrees of freedom while maintaining a high support stiffness in other directions. Hence, thanks to this technique, the stiffnesses ratios, (i.e. the support stiffnesses divided by natural stiffnesses) which is a key performance index used to characterize flexure mechanisms can be increased by several orders of magnitude. Additionally, the natural stiffness value of the whole mechanism can be adjusted to be positive, close to zero or negative (bistable behavior), and can be made independent of temperature variation (remark 4). Lastly, the PCM provides preload and compliance by design, meaning that it is manufactured monolithically in a preloaded state without requiring any additional components dedicated to preloading. This implies that it is very suitable for large-scale production, while solving one of the major drawbacks of flexible mechanisms which is their intrinsic stiffness. This preloading approach which is applicable for various materials and scales has potential applications typically in MEMS and mechanical watchmaking.

To investigate this novel technique, monocrystalline silicon mechanisms permanently prestressed by thermal oxidation are fabricated and experimentally tested. Firstly, fixed-fixed buckled beam deflection magnitudes are compared with and without the integration of a PCM in order to evaluate the preloading performances. In a second stage, we examine the PCM applicability in prestressing buckling-based flexure linear stages for stiffness reduction. Based on an analytical model established in this paper, three types of translational stiffnesses are designed: reduced positive stiffness; near-zero positive stiffness; and negative stiffness. Finite element model (FEM) is carried out to verify the design of the mechanisms. The translational stiffness of the different flexure linear stages is measured and compared to a non-preloaded equivalent stage to estimate the stiffness reduction. The stage operating stroke (i.e. actuation region where the stiffness remains constant), which is directly linked to the preloading level of the PCM, is also experimentally evaluated.

Section 2 presents the design concepts of the PCM, then mechanisms used to assess the performances of the conceptual designs are described and analytically modeled in sections 3 and 4, respectively. The technological implementation, including the design of the fabricated mechanisms and the manufacturing process, is explained in section 5. The FEM modeling and the experimental methods are explained in sections 6 and 7, respectively. All the results are given and discussed in sections 8. Finally, a conclusion of this research is provided in section 9.

2. PCM

The PCM (figure 2) is based on a displacement amplification mechanism, called chevron, which is known for its use as means to amplify the stroke of MEMS actuators (usually based on beam thermal expansion by Joule heating) [28–31] or as test structures to measure residual stress [32, 33]. In our case, this structure is used to amplify the longitudinal strain of beams generated by residual stress. In the present paper, the chevron mechanism uses residual stress to permanently preload other compliant mechanisms. More particularly, the residual stress is caused by thin films grown on all the surfaces of the mechanism during the fabrication process.

The PCM consists of a stage sustained by an array of initially straight inclined beams (called preloading beams) that are mirrored about the stage central axis (see figure 2(a)). Compressive residual stress applied to all the beams is used to elongate them by an increase ΔL_p generating in turn a unidirectional amplified displacement Δx (see figure 2(b)). The motion direction and the amplification ratio $\Delta x/\Delta L_\mathrm{p}$ depend on the inclination angle α. When α is set close to zero, the amplification ratio is high but consequently the preloading force P_x is low. Note that the number of preloading beams n can be increased to apply higher preloads P_x.

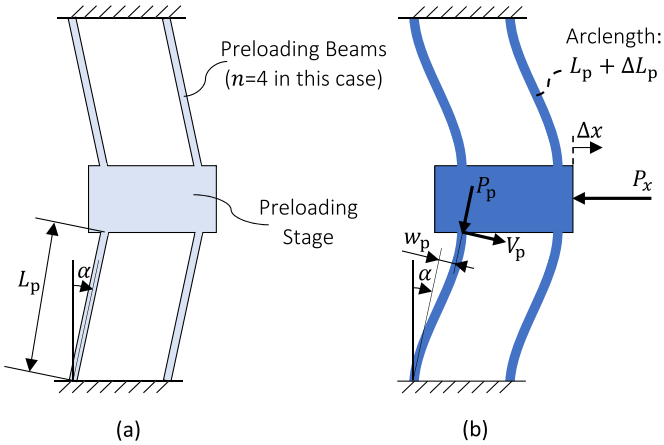

Figure 2. PCM: preloading chevron mechanism before (a) and after (b) residual stress is applied. Note that P_x is an external force applied to the PCM, whereas P_p and V_p are internal forces applied to one of the preloading beams.

Remark 1. This mechanism can also be preloaded by tensile residual stress. In this case, the amplified motion Δx of the preloading stage happens in the opposite direction. For example, silicon nitride can be deposited with low pressure chemical vapor deposition (LPCVD) on a silicon substrate to exhibit a tensile residual stress as high as 1 GPa. Although any other material may be grown or coated on the PCM, the thin film needs to be conformal and apply high residual stress for more effective preloading.

3. Selected mechanisms for performance testing

To evaluate the performances of the PCM, we model and experimentally test three types of mechanisms preloaded by thin film residual stress:

(1) Simple buckled beam (SBB).
(2) PCM-preloaded buckled beam (PBB).
(3) PCM-preloaded linear stage (PLS).

The SBB is based on an initially straight beam fixed to the substrate fixed frame at both extremities (figure 3(a)). The beam buckles from the residual stress of their own thin film (figure 3(b)). The SBB is an existing test structure that can be used to evaluate the effective residual stress value [1, 3, 34, 35]. Using an array of buckled beams with different geometry parameters provide a more accurate value of the residual stress. To this end, we test SBB with varied lengths in order to evaluate the residual stress applied in all the fabricated mechanisms. For further precision of this measurement and to assess the effect of residual stress on anisotropic material, the beams can be oriented along different crystallographic directions (as explained in section 5).

The PBB is also based on an initially straight fixed-fixed buckled beam. However, the buckled beam is preloaded by a PCM attached at one extremity (figures 3(c) and (d)).

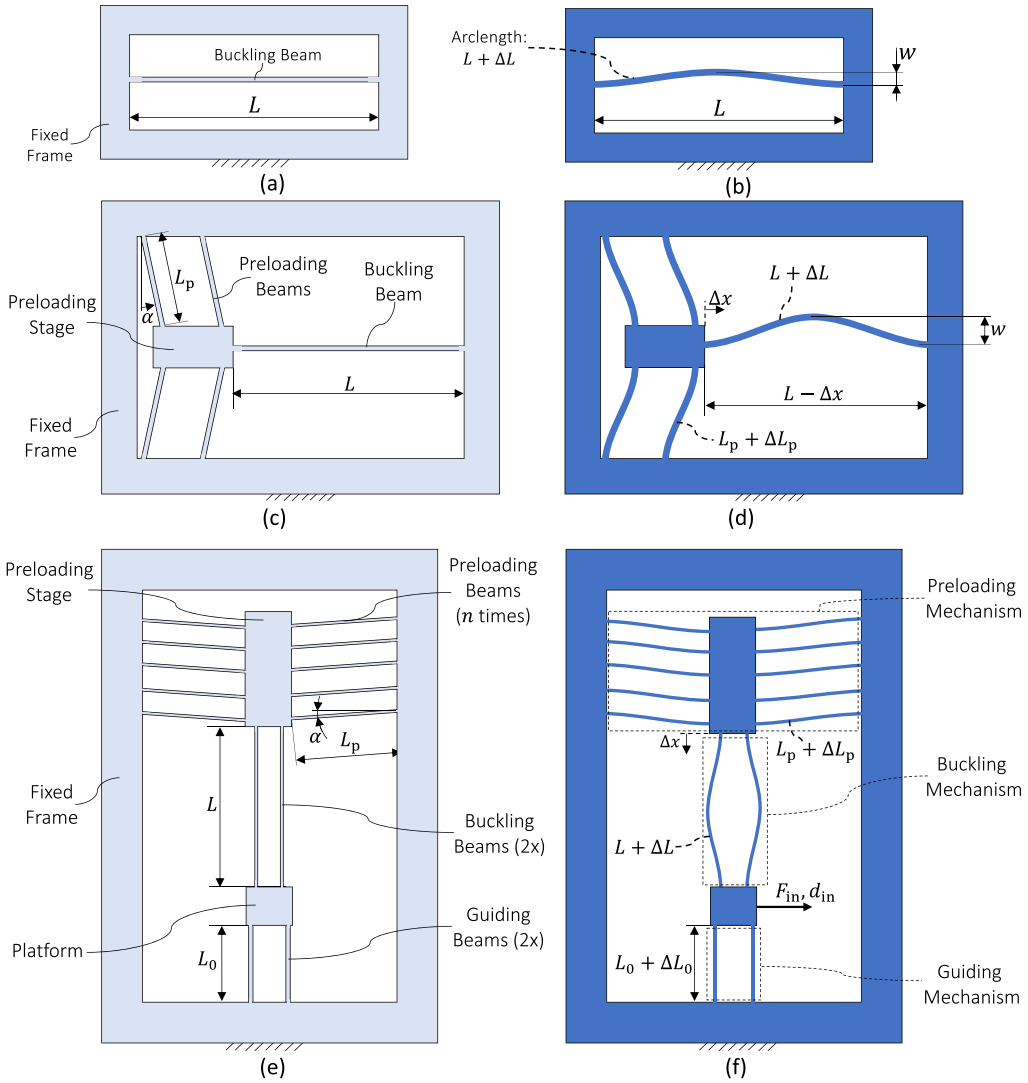

Figure 3. Fabricated mechanisms: (1) SBB: simple fixed-fixed buckling beam (a) before (b) and after residual stress is applied (2) PBB: fixed-fixed buckling beam preloaded by a PCM before (c) and after (d) residual stress is applied (3) PLS: flexure linear stage preloaded by a PCM before (e) and after (f) residual stress is applied.

Comparing the maximum beam deflection of an SBB and a PBB with equal dimensions allows us to experimentally evaluate the preloading performances of the PCM and the generated gain with respect to a SBB structure.

The PLS consists of a guiding mechanism, a buckling mechanism and a PCM (figures 3(e) and (f)). The guiding mechanism possesses two parallel leaf springs (called guiding beams) attached to the fixed frame that are used to guide the moving platform in translation. The buckling mechanism is composed of two beams (called buckling beams) that are connected in parallel to the platform. These beams are buckled by the preloading displacement Δx applied by a PCM. With fixed-guided boundary conditions, the buckling beams provide a constant negative stiffness at the vicinity of the neutral position (i.e. $d_{\text{in}} = 0$) [36–41], reducing the positive stiffness of the guiding beams. Therefore, depending on the dimensions of the guiding and buckling beams, the total stiffness value $F_{\text{in}}/d_{\text{in}}$ of the platform around $d_{\text{in}} = 0$ is either: reduced positive (stiffness tuning); near-zero (zero-force characteristics); or negative (bistable behavior). PLS with different stiffnesses are manufactured and tested, to verify the working principle of the PLS mechanism, but also to demonstrate the applicability of the PCM to preload flexure mechanisms. Indeed, the stroke of the PLS (where the stiffness is reduced) is directly dependent on the preloading displacement Δx.

4. Analytical modeling

This section provides an analytical model of the selected mechanisms. In section 4.1, we derive a general formula of the length variation of a beam being prestressed by thin film residual stress and loaded by external compression. Based on the obtained formula, the deflections of the SBB, PCM and PBB mechanisms are then computed in sections 4.2–4.4, respectively. Finally, the force-displacement characteristics of

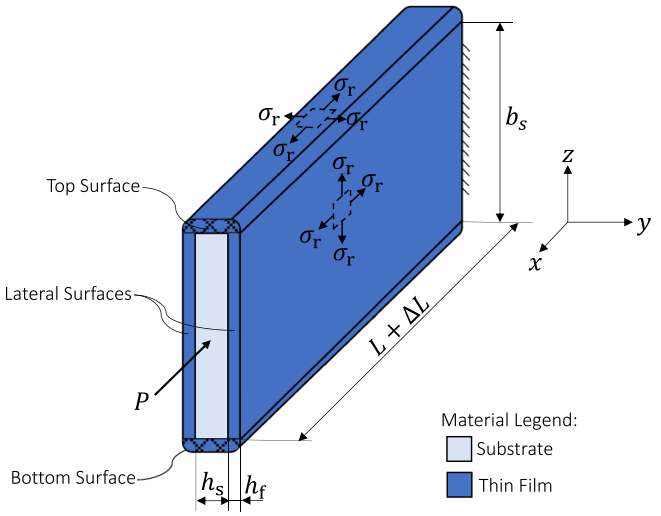

Figure 4. Beam length variation ΔL resulting from thin film equi-biaxial compressive residual stress σ_r and external longitudinal force P.

a fixed-guided buckled beam is analyzed in section 4.5 and then used in section 4.6 to evaluate the total stiffness of the PLS.

For all the calculations, the following hypotheses are considered:

— The fixed frame, the preloading stage and the platform, having a larger cross-section than the beams, are considered infinitely rigid (and are hence not affected by the film residual stress).
- The influence of gravity is neglected.
- The dynamic effects are ignored.
- The shear stress is neglected.
- The beam materials have linear, elastic and uniform properties.
- The beams are initially straight (or slightly pre-curved).
- All the beams in the mechanisms have the same cross section (both in terms of dimensions and materials).

4.1. Beam length variation

In this section, the length variation ΔL of a beam subject to equi-biaxial thin film residual stress σ_r (here $\sigma_r > 0$ if compressive) and external longitudinal force P is modeled. The beam consists of a substrate core (indexed by s) with initial length L. A thin film (indexed by f) with uniform thickness h_f is grown everywhere around the substrate section. The beam core has a final uniform rectangular cross section $b_s \times h_s$, see figure 4. Assuming that the thickness h_s is substantially smaller than the width b_s, the stiffness and the residual stress in the top and bottom surfaces of the film (i.e. areas shown with cross-hatching in figure 4) are neglected in the model. Also, the residual stress and resulting strain are assumed uniform in the materials.

Considering a biaxial stress state along x and z (i.e. $\sigma_{f,y} = \sigma_{s,y} = 0$) in the lateral surfaces, the compliance matrix of the film and the substrate, respectively $\mathbf{S_f}$ and $\mathbf{S_s}$, can be reduced into 2×2 dimensions. The strain–stress relationships are then given by:

$$\begin{pmatrix} \varepsilon_{f,x} \\ \varepsilon_{f,z} \end{pmatrix} = \mathbf{S_f} \begin{pmatrix} \sigma_{f,x} \\ \sigma_{f,z} \end{pmatrix}, \begin{pmatrix} \varepsilon_{s,x} \\ \varepsilon_{s,z} \end{pmatrix} = \mathbf{S_s} \begin{pmatrix} \sigma_{s,x} \\ \sigma_{s,z} \end{pmatrix} \tag{1}$$

where:

$$\mathbf{S_f} = \begin{pmatrix} \frac{1}{E_{f,x}} & \frac{-\nu_{f,zx}}{E_{f,z}} \\ \frac{-\nu_{f,xz}}{E_{f,x}} & \frac{1}{E_{f,z}} \end{pmatrix}, \mathbf{S_s} = \begin{pmatrix} \frac{1}{E_{s,x}} & \frac{-\nu_{s,zx}}{E_{s,z}} \\ \frac{-\nu_{s,xz}}{E_{s,x}} & \frac{1}{E_{s,z}} \end{pmatrix}. \tag{2}$$

The Young's modulus (E) and Poisson's ratio (ν) are expressed with respect to the axes of interest (x, z) and component (f, s). The stress in the film is related to the compression residual stress σ_r (assumed constant for both x and z directions) and the elastic stress applied by the substrate:

$$\begin{pmatrix} \sigma_{f,x} \\ \sigma_{f,z} \end{pmatrix} = \begin{pmatrix} \sigma_r \\ \sigma_r \end{pmatrix} - \gamma \begin{pmatrix} \sigma_{s,x} \\ \sigma_{s,z} \end{pmatrix} \tag{3}$$

where $\gamma = \frac{h_s}{2h_f}$. Assuming that the beam strain along x and z are respectively equal between the film and the substrate (i.e. $\varepsilon_{f,x} = \varepsilon_{s,x} = \varepsilon_x$, $\varepsilon_{f,z} = \varepsilon_{s,z} = \varepsilon_z$) and using equations (1) and (3), the beam strain is related to the residual stress by:

$$\begin{pmatrix} \varepsilon_x \\ \varepsilon_z \end{pmatrix} = \mathbf{S_s}(\mathbf{S_s} + \gamma \mathbf{S_f})^{-1} \mathbf{S_f} \begin{pmatrix} \sigma_r \\ \sigma_r \end{pmatrix}. \tag{4}$$

We then define the effective elastic modulus as $E_{eff,x} = \sigma_r / \varepsilon_x$, computed from equation (4), linking the beam longitudinal strain to the residual stress. In case the film material is isotropic ($E_{f,x} = E_{f,z} = E_f$ and $\nu_{f,xz} = \nu_{f,zx} = \nu_f$) and the substrate material is orthotropic ($\nu_{s,xz} = \nu_{s,zx} E_{s,x} / E_{s,z}$), $E_{eff,x}$ becomes:

$$E_{eff,x} = \frac{E_f}{1-\nu_f} + \frac{E_{s,z}}{\mu - \nu_{s,zx}}\gamma + \frac{1-\mu}{1-\nu_f} \frac{\mu\nu_f - \nu_{s,zx}}{(\mu - \nu_{s,zx})(1+\nu_f)\rho\gamma - \nu_{s,zx}^2 + \mu} \frac{E_{s,x}}{1-\nu_{s,zx}}\gamma \tag{5}$$

where $\mu = E_{s,z}/E_{s,x}$ and $\rho = E_{s,z}/E_f$. More particularly, if the substrate material has the same Young's modulus along x and z (i.e. $E_{s,x} = E_{s,z}$, thus $\mu = 1$), equation (5) simplifies as:

$$E_{eff,x} = \frac{E_f}{1-\nu_f} + \frac{E_{s,z}}{1-\nu_{s,zx}}\gamma. \tag{6}$$

Finally, considering linear elastic materials, the total beam length variation $\Delta L/L$ is the sum of the beam longitudinal strain resulting from the residual stress σ_r and from the externally applied force P:

$$\frac{\Delta L}{L} = \frac{\sigma_r}{E_{eff,x}} - \frac{P}{(EA)_{tot}} \tag{7}$$

where the equivalent product of the Young's modulus E and the section area A of the composite beam is $(EA)_{tot} = (E_f 2h_f + E_{s,x} h_s) b_s$.

4.2. Deflection of the SBB

We consider that the composite beam presented in section 4.1 is now rigidly attached at both extremities to the substrate fixed frame. With fixed-fixed boundary conditions, the beam can buckle from the residual stress of the film. If the beam is in buckled state, its axial load P is equal to its critical buckling load P_{crit} given by:

$$P_{\text{crit}} = \frac{4\pi^2 (EI)_{\text{tot}}}{L^2} \tag{8}$$

where the equivalent flexural rigidity of the composite beam is $(EI)_{\text{tot}} = E_{\text{f}} I_{\text{f}} + E_{\text{s},x} I_{\text{s}}$, where $I_{\text{f}} = b_{\text{s}} \left((h_{\text{s}} + h_{\text{f}})^3 - h_{\text{s}}^3 \right) / 12$ and $I_{\text{s}} = b_{\text{s}} h_{\text{s}}^3 / 12$ are the quadratic moments of the film and substrate, respectively. The beam buckles if its arclength variation ΔL is bigger than zero. From equation (7), it implies that P_{crit} is smaller than the term $\sigma_{\text{r}} (EA)_{\text{tot}} / E_{\text{eff},x}$. In buckled state, the beam forms an arch (see figure 3(b)) where the deflection is maximum at the middle of the length L and is given by [6] as:

$$w = \frac{2}{\pi} \sqrt{\frac{\Delta L}{L}} L. \tag{9}$$

4.3. Preloading characteristics of the PCM

We now compute the force-displacement characteristics $P_x(\Delta x)$ of the PCM (figure 2). We assume that all the preloading beams have the same dimensions and inclination, and are preloaded by thin film residual stress as described in section 4.1. Geometrically, the preloading displacement Δx is related to the lateral deformation w_{p} and to the arclength elongation ΔL_{p} of each preloading beam:

$$w_{\text{p}} = \Delta x \cos(\alpha) \tag{10}$$

$$\Delta L_{\text{p}} - \lambda_{\text{p}} = \Delta x \sin(\alpha) \tag{11}$$

where $\lambda_{\text{p}} = 3/5 \cdot w_{\text{p}}^2 / L_{\text{p}}$ is the longitudinal shortening of a preloading beam due to its deflection [42, equation (5.13)]. Considering n preloading beams, the external force P_x is a function of the internal forces P_{p} and V_{p}:

$$P_x = n \left(P_{\text{p}} \sin(\alpha) - V_{\text{p}} \cos(\alpha) \right) \tag{12}$$

where P_{p} is obtained using equations (7), (10) and (11):

$$P_{\text{p}} = (EA)_{\text{tot}} \left(\frac{\sigma_{\text{r}}}{E_{\text{eff},x}} - \frac{\Delta x}{L_{\text{p}}} \sin(\alpha) - \frac{3}{5} \left(\frac{\Delta x}{L_{\text{p}}} \right)^2 \cos^2(\alpha) \right) \tag{13}$$

and V_{p} is the lateral force of a preloading beam given by [42, equation (5.39)] and equation (10) as:

$$V_{\text{p}} = \frac{12 (EI)_{\text{tot}}}{L_{\text{p}}^3} \left(1 - \frac{L_{\text{p}}^2 P_{\text{p}}}{\pi^2 (EI)_{\text{tot}}} \right) \Delta x \cos(\alpha). \tag{14}$$

4.4. Deflection of the PBB

To evaluate the deflection magnitude w of a PBB, the preloading displacement Δx can be found by inverting the function $P_x(\Delta x)$ (equation (12)) and substituting $P_x = P_{\text{crit}}$ (equation (8)). Since the buckled beam is both preloaded by the PCM and the residual stress of its own film, the maximum deflection magnitude w given in equation (9) becomes:

$$w = \frac{2}{\pi} \sqrt{\frac{\Delta x + \Delta L}{L}} L. \tag{15}$$

4.5. Actuation characteristics of a fixed-guided buckled beam

In this section, we model the actuation characteristics $F_{\text{in}}(d_{\text{in}})$ of a single fixed-guided buckled beam as shown in figure 5. This analysis will be useful to compute the total stiffness of the PLS (in section 4.6) since it is based on a buckling mechanism with two fixed-guided buckled beams. The formulas are derived from the analytical model of generic buckled beams developed in a previous work [43].

The actuation characteristics of the fixed-guided buckled beam involves two kinds of solutions that we respectively call *First Mode Branch* and *Second Mode Branch*, as they contain the first and second modes of buckling. In First Mode Branch, the stage stiffness $K_{\text{in}} = F_{\text{in}} / d_{\text{in}}$, the axial force P and the input displacement d_{in} can all be parametrized by a nondimensional parameter kL [43] as follows:

$$\begin{aligned} K_{\text{in}} &= \frac{(EI)_{\text{tot}}}{L^3} \frac{(kL)^3}{2\tan\left(\frac{kL}{2}\right) - kL}, P = \frac{(EI)_{\text{tot}} (kL)^2}{L^2}, \\ d_{\text{in}} &= \pm \sqrt{\frac{1}{H(kL)}} \sqrt{\frac{\Delta l}{L}} L \end{aligned} \tag{16}$$

where:

$$H(kL) = kL \frac{2kL - 3\sin(kL) + kL\cos(kL)}{4\left(kL\cos\left(\frac{kL}{2}\right) - 2\sin\left(\frac{kL}{2}\right)\right)^2}. \tag{17}$$

When the parameter kL reaches the value of 2π, it leads to a branch bifurcation to the Second Mode Branch. In Second Mode Branch, the stiffness of the beam is constant and negative, and the axial compression force is constant:

$$K_{\text{in}} = -\frac{4\pi^2 (EI)_{\text{tot}}}{L^3}, \; P = \frac{4\pi^2 (EI)_{\text{tot}}}{L^2}. \tag{18}$$

The maximum stroke where the beam state stays in a Second Mode Branch is given by:

$$d_{\text{in,max}} = \frac{2}{\sqrt{3}} \sqrt{\frac{\Delta l}{L}} L. \tag{19}$$

Parametric curves of the input force F_{in} are plotted as a function of the input displacement d_{in} in figure 5(d). For the First Mode Branch, the graph is plotted by varying the parameter kL from 0 (zero compression state, shown by points

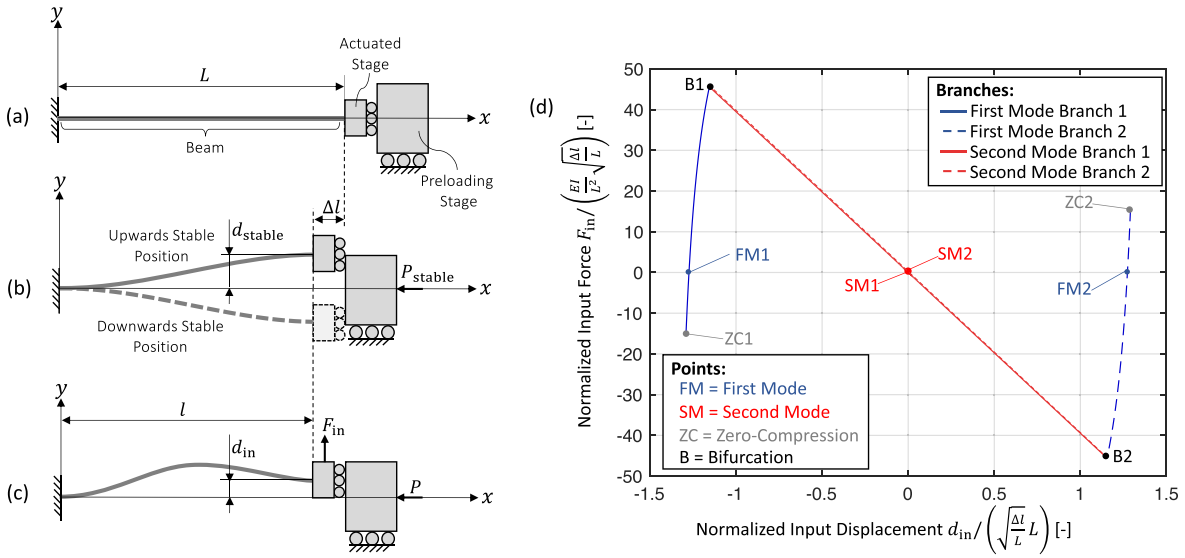

Figure 5. Fixed-guided buckled beam (a) as-fabricated, (b) buckled into one of its two stable positions, (c) deflection when a force is applied to the input stage to switch between its two stable states, and (d) normalized actuation characteristics of the fixed-guided buckled beam.

ZC1 and ZC2) to 2π (bifurcation points B1 and B2). For the Second Mode Branch, d_{in} is ranged from $-d_{\text{in,max}}$ to $d_{\text{in,max}}$. Since there are always two symmetrical solutions for d_{in} (the beam can buckle upwards or downwards), two symmetrical curves (indices 1 and 2) for both types of branches are displayed. Note that Second Mode Branches 1 and 2 correspond to the same force-displacement curve. The first modes FM1 and FM2 correspond to the two stable equilibriums of the bistable buckled beam (figure 5(b)) and are obtained on the First Mode Branches when $kL = \pi$. In this case, the lateral displacement and the axial load are respectively:

$$d_{\text{stable}} = \pm\frac{4}{\pi}\sqrt{\frac{\Delta l}{L}}L,\ P_{\text{stable}} = \frac{\pi^2(EI)_{\text{tot}}}{L^2}. \tag{20}$$

The Second Modes SM1 and SM2 correspond to two unstable equilibriums of the bistable buckled beam and are obtained at the neutral position ($d_{\text{in}} = 0$).

4.6. Stiffness and stroke of the PLS

The total stiffness $K_{\text{in,tot}}$ of the PLS is the sum of the stiffnesses $K_{\text{in,GM}}$ and $K_{\text{in,BM}}$ of the guiding and buckling mechanisms, respectively:

$$K_{\text{in,tot}} = \frac{F_{\text{in,tot}}}{d_{\text{in}}} = K_{\text{in,GM}} + K_{\text{in,BM}}. \tag{21}$$

The guiding mechanism stiffness $K_{\text{in,GM}}$ is expressed in [42, equation (5.39)] as:

$$K_{\text{in,GM}} = \frac{24(EI)_{\text{tot}}}{L_0^3}\left(1 - \frac{L_0^2 N}{2\pi^2(EI)_{\text{tot}}}\right) \tag{22}$$

where N is the axial preload applied on the guiding mechanism by the buckling mechanism. Since the buckling mechanism consists of two fixed-guided buckled beams, $N = 2P$ and $K_{\text{in,BM}} = 2K_{\text{in}}$, where P and K_{in} are given in equation (16) or (18) depending if the fixed-guided buckled beams follow a First or Second Mode Branch, respectively. Around the neutral position (i.e. $d_{\text{in}} = 0$), the buckling beams follows a Second Mode Branch. In this case, the total stiffness is constant and equal to:

$$K_{\text{in,tot}} = \frac{8(EI)_{\text{tot}}}{L_0^3}\left(3 - 12\left(\frac{L_0}{L}\right)^2 - \pi^2\left(\frac{L_0}{L}\right)^3\right). \tag{23}$$

To design a zero-force mechanism, $K_{\text{in,tot}} = 0$ around $d_{\text{in}} = 0$, a beam length ratio $L_0/L = 0.43$ must be selected.

As mentioned previously, the stroke of the PLS depends on the preloading level of the buckling beams. Their end-shortening is given by $\Delta l = \Delta x + \Delta L + \Delta L_0 + \lambda_0$, where $\lambda_0 = -3/5 \cdot d_{\text{in}}^2/L_0$ [42, equation (5.13)] is the parasitic shift of the guiding beams, and the beam length variations ΔL and ΔL_0 are function of the residual stress σ_{r} and the compressive load P following equation (7). Since Δx is function of $P_x = N$ by the relation (18), Δx can also be parametrized by kL. When the buckling beams follows a First Mode Branch, the platform displacement d_{in} expressed in equation (16) becomes:

$$d_{\text{in}} = \pm\sqrt{\frac{\Delta x(kL) + (L + L_0)\cdot\left(\frac{\sigma_{\text{r}}}{E_{\text{eff},x}} - \frac{(EI)_{\text{tot}}(kL)^2}{(EA)_{\text{tot}}L^2}\right)}{\frac{H(kL)}{L} + \frac{3}{5}\frac{1}{L_0}}}. \tag{24}$$

The maximum stroke $d_{\text{in,max}}$ where the total stiffness remains constant (i.e. the stroke of a Second Mode Branch), can be computed by substituting $kL = 2\pi$ in equation (24).

5. Mechanism manufacturing and design

All the mechanisms are produced from monocrystalline (100)-orientated p-type silicon wafers having a thickness

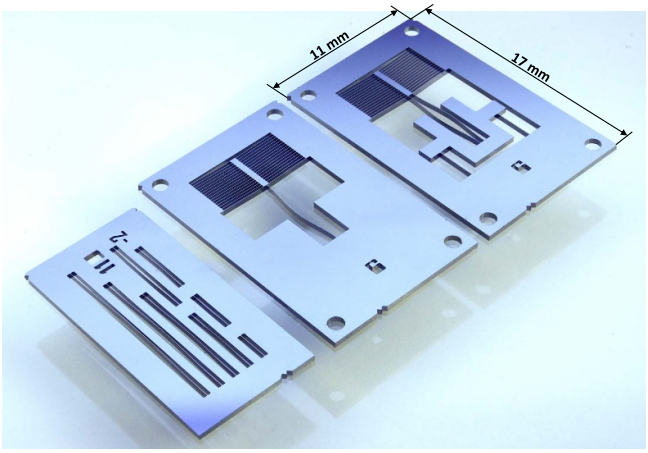

Figure 6. Photograph of the three different types of manufactured oxidized silicon mechanisms. From left to right: set of simple buckled beams (SBB); a buckled beam ($L = 6$ mm) preloaded by a chevron (PBB), flexure linear stage with buckled beams ($L = 6$ mm) preloaded by a chevron (PLS).

of $b_s = 380$ μm. The basic steps of the manufacturing process are the following:

(1) Deep reactive ion etching (DRIE), to fabricate the mechanisms.
(2) Thermal oxidation, to apply residual stress in the mechanisms.

Silicon dioxide is grown on the etched silicon wafers through wet oxidation at 1050 °C and atmospheric pressure. At this temperature, the oxide has a sufficiently low viscosity to easily flow on the wafer, involving a low intrinsic stress [44]. During the cooling of the wafers to room temperature, thermal stress appears in the oxide film, prestressing the different mechanisms permanently. Finally, the different mechanisms are separated by manually breaking flexible links connecting the rigid frame of the mechanisms to the wafers. A picture of the different types of mechanisms is shown in figure 6.

For thermal oxidation of silicon, the film material is isotropic. Young's modulus and the Poisson's ratio of thermal silicon dioxide are respectively given by $E_f = 75$ GPa and $\nu_f = 0.17$ [5]. Since we selected (100)-oriented monocrystal silicon wafers, the z-axis of the beams (see figure 4) is always along the <100> direction, thus $E_{s,z} = 130$ GPa [45]. The longitudinal axis of the beams is oriented along the <100> and <110> crystallographic directions for the SBB. While for the PBB and PLS, only the <100> axis is chosen (or close to this direction for the preloading beams). This orientation is adopted because the Young's modulus is the lowest and thus the preloading effect of the residual stress is the strongest. Indeed, depending on the orientation of the beams, the effective elastic modulus $E_{\text{eff},x}$ varies:

- For beams aligned with the <100> direction, then $E_{s,x} = E_{s,100} = 130$ GPa and $\nu_{s,zx} = 0.28$. Since $E_{s,x} = E_{s,z}$, equation (6) is used to compute $E_{\text{eff},x}$.
- For beams aligned with the <110> direction, then $E_{s,x} = E_{s,110} = 169$ GPa and $\nu_{s,zx} = 0.28$. Since $E_{s,x} \neq E_{s,z}$, equation (5) is used to compute $E_{\text{eff},x}$.

All the beams are designed with the same cross section (final substrate thickness $h_s = 20$ μm and oxide film thickness $h_f = 3$ μm conformally grown, see figure 4) in order to simplify the modeling of the mechanisms. Only the length L of the buckling beams, the length L_p, and the inclination angle α of the preloading beams are varied. The mechanism dimensions (table 1) are selected based on the material parameters and the analytical model provided in section 4.

Eight and six different buckling beam lengths L are selected for the SBB and the PBB, respectively. Two different preloading beam lengths and inclinations α are chosen for the PBB depending on the buckling beam lengths L. For the PBB and PLS, L_p is approximately half of L and the number of preloading beams is limited to $n = 32$, as a mechanism space constraint. For all the PCM, the gap between two consecutive preloading beams is set to 200 μm (estimated technological limit of DRIE). The compression applied in each preloading beam must not exceed its fixed-fixed critical buckling load $P_{p,\text{crit}}$ (given in equation (8) using $L = L_p$), otherwise, the whole PCM, whose structure is bistable [46], will snap to its second stable mode. Depending on the force P_x applied by the buckling beams on the PCM, α is adjusted using equation (13) to always ensure that $P_p < P_{p,\text{crit}}$ with a reasonable safety margin of approximately 50%. The initial horizontal projections of the preloading beams are selected as $x_p = L_p \sin(\alpha) = 0.05$ mm for all the PBB (one buckling beam is used) and $x_p = 0.1$ mm for all the PLS (two buckling beams are used). The resulting values of preloading beam lengths L_p and inclinations α are provided in table 1.

The buckling beams of the PLS are slightly pre-curved (20 μm center offset) to force the direction of buckling in opposite directions (in order to minimize the reaction moment applied by the buckling beams to the platform). Three buckling beam lengths are selected to test different actuation characteristics: negative stiffness ($L = 5$ mm), near-zero positive stiffness ($L = 6$ mm) and reduced positive stiffness ($L = 7$ mm). The guiding and preloading beams of the PLS have a fixed length (respectively $L_0 = 2.59$ mm and $L_p = 3$ mm). A non-preloaded equivalent flexure linear stage is also fabricated to evaluate the stiffness reduction of the PLS. All the flexure linear stages have two mechanical stops on the fixed frame used to restrain the platform stroke d_{in} to ± 0.25 mm. This range of motion limits the mechanism deflection so that the stress does not surpass the failure strength of silicon and silicon dioxide, which we estimate to be 800 MPa. Designs where $L \leqslant L_0$ are avoided for beams with same cross section and material, because the support stiffness of such linear stages would be drastically reduced along the beam longitudinal axis. Indeed, the critical load of the buckling beams should not exceed the

Table 1. Design parameters of the mechanisms.

Mechanism	Variants	Buckling beam	Preloading beam		Guiding beam	
		Length L (mm)	Length L_p (mm)	Inclination α (deg)	Length L_0 (mm)	Number of identical samples
Simple buckled beam (SBB)	<100> direction	2, 3, 4, 5, 6, 8, 10, 12	—	—	—	4
	<110> direction	2, 3, 4, 5, 6, 8, 10, 12	—	—	—	4
Preloaded buckled beam (PBB)	'Small' PCM	5, 6, 7	3	0.95	—	2
	'Large' PCM	8, 10, 12	5	0.57	—	2
Flexure linear stage	Preloaded (PLS)	5, 6, 7	3	1.91	2.59	1
	Non-preloaded	—	—	—	2.59	1

critical load of the guiding beams, otherwise the linear stage would lose its guiding function.

6. FEM simulations

In order to verify the characteristics of the SBB, the PBB and the PLS analytically derived in section 4 and to validate their sizing carried out in section 5, FEM studies are conducted using the commercial software COMSOL Multiphysics 6.1. The stationary solver uses the Solid Mechanics module and the Geometric Nonlinearity setting to capture large deformation, buckling and snap-through behaviors. The Segregated approach is used to facilitate the convergence of the solver. All the mechanisms with the dimensions given in table 1 are simulated.

Due to the planar nature of the mechanisms and an interest for rapid numerical calculations, 2D studies are carried out. By selecting 'plane stress' as the 2D approximation setting, it follows that $\sigma_{f,z} = \sigma_{s,z} = 0$ by definition, and therefore Poisson's effect along the z-axis is not considered in the FEM model. Substituting $\nu_f = \nu_{s,zx} = 0$ in equation (5), we obtain an effective elastic modulus in the 2D plane stress simulation which is different from the analytical model:

$$E_{\text{eff},x,2D} = E_f + E_{s,x}\gamma. \tag{25}$$

Note that equation (25) holds for both <100> and <110> directions. To obtain equivalent beam strains from residual stress between the analytical model (3D) and the FEM simulation (2D), we set a corrected residual stress value $\sigma_{r,2D}$ in the FEM software, which is given by:

$$\sigma_{r,2D} = \frac{E_{\text{eff},x,2D}}{E_{\text{eff},x}}\sigma_r \tag{26}$$

where $E_{\text{eff},x}$ is obtained analytically with equation (5) or (6), respectively for <110> and <100> crystal directions. As we consider a plane stress model, $\sigma_{r,2D}$ is only applied along the longitudinal axis of the mechanism beams. The module 'external stress' is used to apply the uniaxial stress $\sigma_{r,2D}$ in the beam oxide domains. The value of $\sigma_{r,2D}$ that is entered in the FEM software is the residual stress σ_r, obtained experimentally (as explained in section 8.2), substituted in the correction formula (equation (26)). A negative sign is employed since the applied stress is compressive.

All the beams are meshed with quadrilateral shell elements such that two elements are mapped across the silicon thickness h_s, one element for each oxide thickness h_f, and one element every 20 μm along the length. The material parameters of the silicon core and the oxide layers are the same as for the analytical model (see section 5).

For all the mechanisms, the simulation is divided into two successive sub-studies:

- **Study 1:** A lateral force of 0.1 N is applied to the side of the buckling beams to force their buckling in a given direction. This study is performed to speed-up the convergence of the solver and avoid unrealistic modes of buckling.
- **Study 2:** Reusing the solution of Study 1 and removing the lateral force, the mechanisms are deflected in stable equilibrium. The maximum deflection of the buckled beam is then extracted for the SBB and PBB. The translation stiffness of the PLS is obtained by varying the lateral position d_{in} of a rigid connector attached to the platform and evaluating the reaction force F_{in}. For each mechanism, the simulated von Mises stress is verified to be less than the estimated failure strength (i.e. 800 MPa).

To evaluate the effect of the mechanism fixed frame stiffness, the PBB and the PLS were simulated with either: a frame considered infinitely rigid (see figure 7(a)); or considering the actual manufactured frame shape and with the elastic parameters of silicon (see figure 7(b)).

7. Experimental method

7.1. Electronic microscope measurements

A scanning electronic microscope (SEM) was used to measure the thicknesses of the silicon core and the silicon dioxide film of the fabricated beams. Since all the beams of the

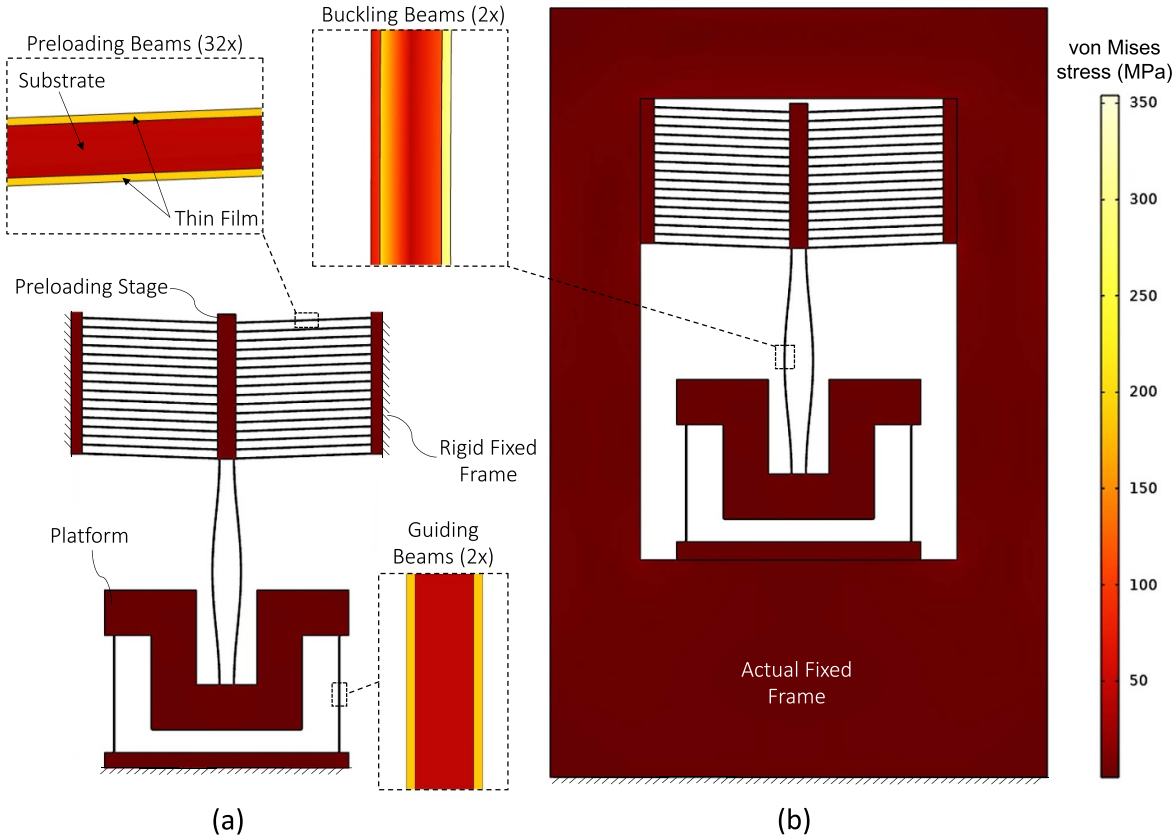

Figure 7. FEM simulation of the PLS with a buckling beam length of $L = 5$ mm placed in neutral position, considering that the mechanism fixed frame is (a) fully rigid or (b) elastic (same material and dimensions as fabricated). Insets show the von Mises stress distribution at the center of the different beams.

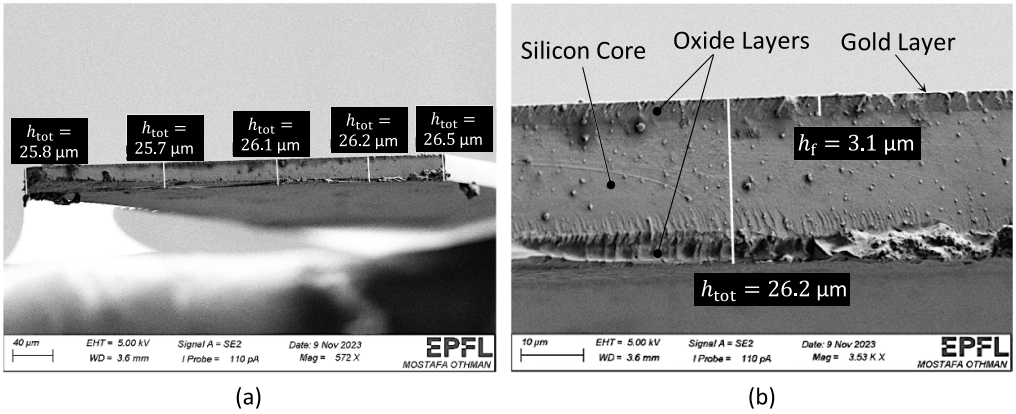

Figure 8. SEM images of the beam sample. (a) Full cross section with distributed thickness measurements and (b) magnified view on one of the measurements.

manufactured mechanisms have the same specified cross section dimensions, the beam from an SBB aligned with the <110> crystal direction was randomly selected as a sample. It is assumed that the measurement results of this sample apply to any mechanism beam, because all the mechanisms were manufactured at the same time under equivalent process conditions. The beam sample was cut approximately at the middle of the length to observe the cross section. A very thin layer of gold (30 nm) was coated on one lateral side of the beam to obtain a better image contrast.

The whole cross-section picture is presented in figure 8(a). Magnified views were taken on five spots along the beam width, to see if the beam section has a potential trapezoidal shape [47]. At each spot, the thicknesses of the substrate and film were recorded with a measurement resolution of ± 0.1 μm. Figure 8(b) shows the measurement performed at

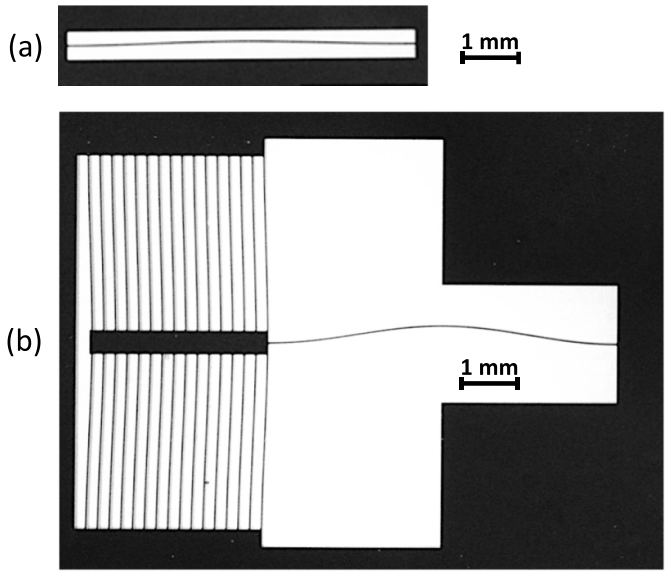

Figure 9. Photographs (top view) of (a) SBB and (b) PBB mechanisms having both a buckled beam length of $L = 6$ mm.

one of the spots. The measurement results are directly reported in figure 8(a) and discussed in section 8.1.

7.2. Optical microscope measurements

The deflection shapes of the buckled beams of the SBB and the PBB were measured under an optical microscope, see figure 9. For each beam, the deflection magnitude at the middle of the beam length was recorded. The measurement uncertainty of the deflection magnitude is evaluated as ± 1 μm.

7.3. Stiffness measurements

A dedicated test bench was realized in order to measure the force-displacement characteristics of the PLS and the non-preloaded linear stage. The test bench, presented in figure 1, primarily consists of a manual translation stage used to control the displacement d_{in} of the mechanism platform. An actuating pin (ø1 mm), fixed on a pin holder, is used to push or pull the platform depending on the actuation direction (see inlet in figure 10). An additional vertically oriented manual micro positioning stage helps to pass the pin above the mechanism platform in order to switch the actuation direction. The actuation force F_{in} is measured using a force sensor (Futek LPM200) placed between the manual translation stage and the pin holder. A laser displacement sensor (Keyence LK-H082) measures the platform displacement d_{in}. The equipment and the tested mechanism are rigidly fixed to an optical table. The silicon mechanism plane is perpendicular to the direction of gravity to avoid measuring gravity-related forces.

Before starting the experiment, the neutral position of the mechanism, defined as F_{in}-d_{in} graph origin, is recorded. For PLS having a positive stiffness, this position is obtained when the force sensor (previously calibrated and tared) starts to return a non-zero value. For the PLS with negative stiffness, the neutral position is assessed when the platform suddenly snaps to the opposite stable position. The experiment starts by displacing the platform by constant gradual displacement steps from the neutral position. At each displacement increment, the force and displacement sensor readings are recorded. All measurements are taken when the system is at static equilibrium to avoid dynamic effects. The experiment ends when the platform reaches a mechanical stop or when the negative stiffness PLS stays at one of its two stable positions. The mechanisms are characterized in both directions with respect to the neutral position. All the force measurements are averaged over five repetitions to reduce measurement noise. The measurement results are reported in section 8.4. The measurement uncertainty corresponds to ± 10 μN for the actuation force F_{in}, and ± 2 μm for the platform displacement d_{in}.

8. Results and discussion

8.1. Beam thickness verification

The beam thickness measurements are shown in figure 8(a) with respect to the five locations along the beam width. The beam total thickness increases from 25.8 μm to 26.5 μm (from top to bottom surfaces of the wafer). This creates a trapezoidal-like cross section which is commonly observed in silicon beams manufactured with DRIE process [47]. The mean value and standard deviation of the total thickness are respectively 26.1 μm and 0.3 μm. The measured thickness of the oxide film has a mean value of 3.1 μm for a resolution of ± 0.1 μm. In addition, the oxide thickness has been verified with ellipsometry on a blanket wafer and the tolerance is overall below 50 nm. Note that the oxide thickness is slightly different depending of the silicon crystal orientation (+60 nm difference for <110> compared to <100> based on Deal–Grove model). In conclusion, we may infer that there is considerable concordance between the measurements and the specified thicknesses, i.e. $h_{\text{tot}} = h_{\text{s}} + 2h_{\text{f}} = 26$ μm and $h_{\text{f}} = 3$ μm.

8.2. Residual stress measurement

The measured deflection magnitude w of the SBB is normalized and plotted in figure 11(a) as function of the beam length L. The measurements are relatively repeatable; indeed, the maximum standard deviation of the measured deflection magnitude w is 4 μm (obtained with the <100>-oriented beams having a length of $L = 12$ mm). Figure 11(a) shows that the buckled beams do not buckle for lengths under $\sim$2 mm, because the residual stress is not sufficient to obtain a positive beam arclength variation ΔL (see equation (7)). As expected, <100>-oriented SBB show a larger defection magnitude than the ones oriented along <110>.

We use the following method to measure the actual residual stress in the silicon oxide: the value of σ_{r} is varied in the analytical model until the deflection magnitude of the SBB (equation (9)) fits the experimental data for both <100> and <110> beam orientations. From this method, a residual stress

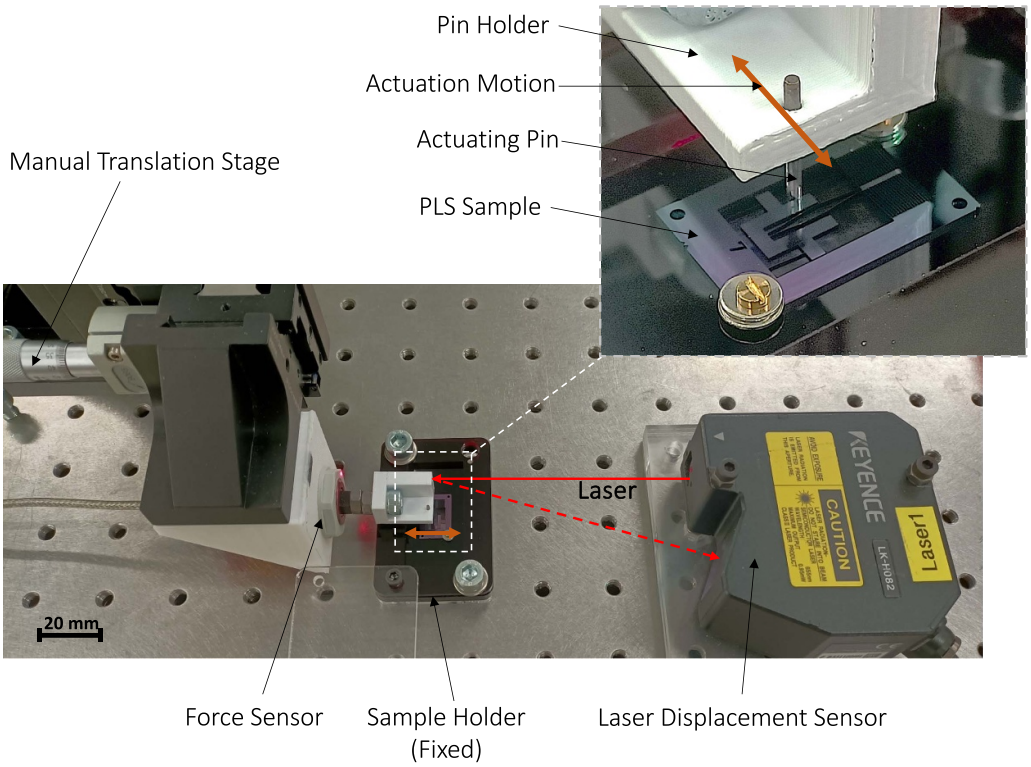

Figure 10. Picture of the test bench used to measure the force-displacement characteristics of the PLS mechanisms.

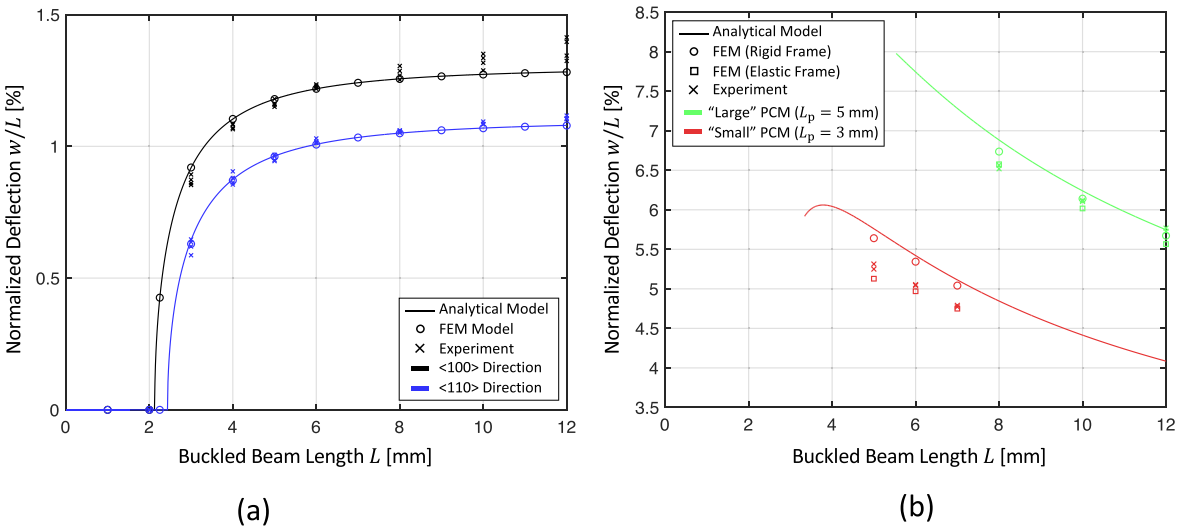

Figure 11. Normalized deflection as a function of the buckled beam length for (a) SBB and (b) PBB mechanisms.

(equi-biaxial) equal to −290 MPa is selected. Based on the approach proposed in section 6, the corrected (uniaxial) residual stress value entered in the FEM software, provided by equation (26), is −213 MPa and −191 MPa for <100> and <110> oriented beams, respectively.

The analytical and FEM results are added in figure 11(a) to evaluate the consistency of the data. The analytical model is validated since the relative error is bounded within 3% and 10% with the FEM and the measurement data, respectively. Since the analytical and simulated values of the residual stress are in excellent agreement with the experiment, these values will be used to model the other manufactured mechanisms.

Remark 2. Further data analysis shows that when the beam length increases, the deflections seem to have higher experimental values than what is predicted by the models. This might be because longer buckled beams have lower buckling compression, which reduces the possibility of plastic deformations during the post-oxidation cooling process. This would then result in higher residual strain of the beams. Additionally,

the fixed frame near the beam extremities may deform less for longer beams (lower compression load) resulting in higher deflection magnitudes. However, since the deflection measurement is less repeatable for long beams, we cannot accurately verify these hypotheses.

8.3. Buckling deflection amplification through PCM integration

The experimental deflections w of the PBB are normalized and plotted in figure 11(b) with respect to the buckling beam length L. The analytical and FEM models are also provided by using the residual stress value that was previously measured in section 8.2. It can be noticed that the analytical model is in good agreement with the FEM study that considers a rigid frame. This is because both these models assume an infinitely stiff frame. On the contrary, the experiment results are strongly consistent with FEM model when the actual (elastic) stiffness of the fixed frame is considered. Simulated deflection magnitudes are decreased by up to 10% when considering that the fixed frame is elastic instead of rigid. This demonstrates that the fixed frame stiffness has a real impact on the deflection level.

Even if the designed fixed frame lacks stiffness, the integration of a PCM to preload a fixed-fixed buckled beam advantageously results in significantly larger deflections. Indeed, figure 11 demonstrates that PBB have experimental deflection magnitudes up to 5 times higher than corresponding SBB (for instance when comparing SBB and PBB having a buckled beam length $L = 8$ mm).

Remark 3. The drawback of integrating a PCM might be that it significantly increases the structure size, as seen in figure 9. However, to achieve the same deflection magnitude, the buckled beam of a SBB must be approximately 5 times longer than the one of a PBB. Additionally, we should note that it is possible to minimize the size of the PCM by bringing its preloading beams closer to each other, thus reducing the gap width from 200 μm to 30 μm, which is feasible with DRIE. To further reduce its size, parametric or topological optimization might be carried out.

8.4. Measured stiffness reduction and stroke of the PLS

The stiffness measurements of the different flexure linear stages are plotted in figure 12 along with the analytical and FEM models. The analytical force-displacement characteristics of the PLS is plotted using equations (21) and (24) for the First Mode Branches (nonlinear stiffness region) by varying kL from 0 to 2π, and using equation (23) for the Second Mode Branches (constant stiffness region). The actuation stiffness of the non-preloaded stage is constant and equal to $24(EI)_{\text{tot}}/L_0^3$ (equation (22) where the axial load $N = 0$).

Figure 12 shows that all the results are mostly consistent between the models and the measurements in the constant stiffness regions. However, in the nonlinear stiffness region, the measured maximum stroke $d_{\text{in,max}}$ of the different PLS

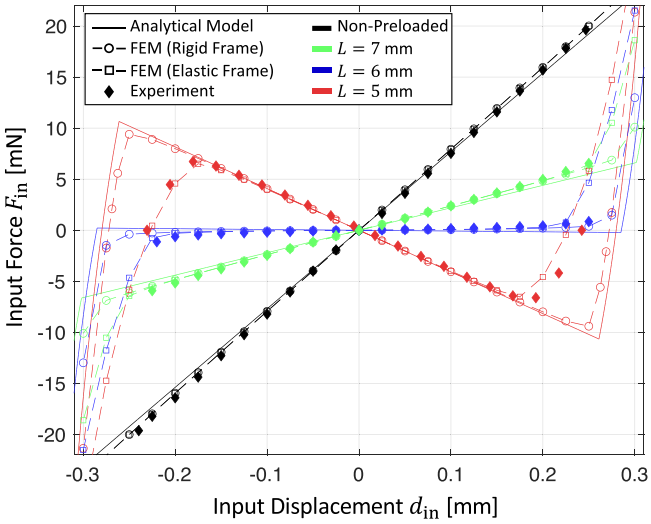

Figure 12. Force-displacement characteristics of the different PLS in comparison to the non-preloaded stage.

is up to 30% lower than the theoretical values. This can be explained by the FEM simulation results where both rigid and elastic fixed frames are considered. The analytical model is in good agreement with the FEM study that considers a rigid frame, because both these models assume an infinitely stiff fixed frame. Whereas the experimental data is rather consistent with the elastic frame FEM results which correspond more closely to the real case. This makes it clear that the fixed frame stiffness has a high impact on the stroke of the PLS.

We can also notice that the experimental data of the near-zero stiffness ($L = 6$ mm) and the negative stiffness ($L = 5$ mm) do not symmetrically follow the FEM results. This could mean that the neutral position of the stage is a bit shifted. This small stiffness asymmetry is assumed to result from manufacturing tolerances and plastic deformation created during the cooling of the oxidized silicon wafers. Indeed, plastic strain can have a consequent impact on the stiffness symmetry of a silicon flexure linear stage preloaded by thermal oxidation as was already observed in [4].

The concept of stiffness reduction is demonstrated experimentally. Indeed, the PLS with a buckling beam length of $L = 7$ mm is reduced by approximately 70% with respect to the non-preloaded linear stage. We have also designed and fabricated a near-zero positive stiffness linear stage (PLS with $L = 6$ mm) with a significant stiffness reduction of 98% (measured stiffness constant is decreased from 78.9 N m^{-1} to 1.87 N m^{-1}). Furthermore, the possibility to manufacture a bistable linear stage having a constant negative stiffness region is demonstrated by using shorter buckling beams ($L = 5$ mm).

Thanks to the PCM, the stroke of the PLS is considerably higher than if the buckling mechanism was only preloaded by the thin film residual stress of the buckling and guiding beams. Indeed, if $\Delta x = 0$ is substituted in equation (24), the stroke of linear stages with equal dimensions but without PCM would be approximatively three times lower.

Remark 4. As the PCM has the same structure as chevron electrothermal actuators, temperature impacts the behavior of the PLS. Indeed, the temperature does affect the residual stress, which is mostly thermal stress, which in turn modifies the preloading displacement Δx. This only alters the platform stroke $d_{\text{in, max}}$, but the total stiffness $K_{\text{in, tot}}$, which is independent of the residual stress value (see equation (23)), is therefore not directly impacted by temperature. The stiffness of the PLS is only slightly modified by the fact that the Young's modulus of the substrate and the thin film are dependent on the temperature. It is however possible to select specific h_s to h_f ratios or coat additional layers of material (e.g. silicon nitride or metal) to compensate the influence of temperature on the beam stiffness while controlling the applied residual stress [48].

8.5. Applicability of the approach

In this paper, we only introduce our method by preloading a simple flexure linear stage. However, the PCM could be used as a building block to preload any sort of compliant structure (e.g. bistable grippers [49] or flexure pivots [50, 51]). For instance, instead of placing the guiding beams in parallel, they could be arranged perpendicularly to create a so-called Remote Center of Compliance (RCC) pivot having a reduced angular stiffness thanks to the PCM. Further types of mechanisms could be designed based on these following proposed guidelines:

(1) Design the guiding mechanism (linear stage, pivot, gripper mechanism, etc) using compliant mechanism design methods [42, 52, 53].
(2) Design the buckling beams (length and boundary conditions) to obtain the requested stiffness reduction, using buckled beam actuation models [43, 54, 55].
(3) Design the PCM (number of preloading beams n, length L_p and inclination α) based on the analytical model and the design method presented in sections 4 and 5, respectively.
(4) Depending on the application, parametric or topology optimization could be performed to adjust the stiffness, maximize the stroke and optimize the mechanism size.

This method can be advantageously applied to create low-voltage microelectromechanical actuators (e.g. comb-drives [23]), high-sensitivity physical sensors (e.g. accelerometers [56], inclinometers [57] and magnetometers [58]), low-frequency energy harvesting structures [8, 59], and low-frequency oscillators for MEMS [23] and mechanical watch regulators [47, 60].

9. Conclusion

The present research introduces a new preloading mechanism based on a chevron beam architecture, called PCM, which is used to amplify the prestressing effect of thin film residual stress. The working principle of this novel design concept is demonstrated by experimenting flexure mechanisms fabricated from silicon substrate and prestressed by thermal oxidation. The mechanisms were designed through analytical and numerical models which are consistent with the experimental results. We found that, in comparison to direct oxide film prestressing, fixed-fixed silicon buckled beams may exhibit a deflection magnitude that is 5 times greater if a PCM is integrated. Furthermore, we show that the translational stiffness of parallel leaf spring stages can be reduced when combined with two fixed-guided buckled beams preloaded by a PCM. For instance, a linear stage with near-zero positive stiffness was experimented, showing a stiffness reduction of 98% compared to an equivalent non-preloaded stage. It is also possible to create a linear stage with bistable behaviors in which the stiffness is sufficiently decreased to become negative. The preloaded linear stages have a relatively large stroke (more than 0.4 mm travel for 2.59 mm leaf spring length) thanks to the amplified preloading displacement generated by the PCM.

This approach of amplifying the residual stress effect could be used to permanently preload other types of compliant mechanisms (e.g. flexure pivots, bistable micro grippers). Such concepts pave the way to manufacturing low stiffness compliant mechanisms for application in MEMS and watchmaking. These structures could be fabricated at different scales and from other substrate and thin film materials. It is even possible to conceive prestressing mechanisms with materials exhibiting tensile residual stresses (e.g. silicon nitride deposited on silicon). In this case, the orientation of the PCM with respect to the buckled beams must be inverted.

Data availability statement

All data that support the findings of this study are included within the article (and any supplementary files).

Acknowledgment

We gratefully thank Marijn Nijenhuis, who was Visiting Professor at Instant-Lab EPFL, for his precious comments on the analysis of the experimental data. We are thankful for the assistance with the SEM visualizations provided by our EPFL colleagues Mostafa Othman, Aïcha Hessler-Wyser, and Morgan Mc Kay Monroe.

ORCID iDs

Loïc Tissot-Daguette https://orcid.org/0000-0003-4031-9668
Florent Cosandier https://orcid.org/0009-0002-4802-731X
Yves Pétremand https://orcid.org/0009-0000-4607-8602
Michel Despont https://orcid.org/0000-0003-3759-2161
Simon Henein https://orcid.org/0000-0002-8441-7772

References

[1] Chen K S 2006 *Techniques in Residual Stress Measurement for MEMS and Their Applications MEMS/NEMS* ed C T Leondes (Springer) (https://doi.org/10.1007/0-387-25786-1_33)

[2] Carneiro J O, Teixeira V and Azevedo S 2014 Residual stresses in thin films evaluated by different experimental techniques *Encyclopedia of Thermal Stresses* ed R B Hetnarski (Springer)

[3] Huff M 2022 Review paper: residual stresses in deposited thin-film material layers for micro- and nano-systems manufacturing *Micromachines* **13** 2084

[4] Kuppens P R, Herder J L and Tolou N 2019 Permanent stiffness reduction by thermal oxidation of silicon *J. Microelectromech. Syst.* **28** 900

[5] Hälg B 1990 On a nonvolatile memory cell based on micro-electro-mechanics *IEEE Proc. on Micro Electro Mechanical Systems, an Investigation of Micro Structures, Sensors, Actuators, Machines and Robots (Napa Valley, CA, USA)* pp 172–6

[6] Vangbo M and Bäcklund Y 1998 A lateral symmetrically bistable buckled beam *J. Micromech. Microeng.* **8** 29

[7] Pan D, Wu Z, Dai F and Tolou N 2020 A novel design and manufacturing method for compliant bistable structure with dissipated energy feature *Mater. Des.* **196** 109081

[8] Xu R, Akay H and Kim S-G 2019 Buckled MEMS beams for energy harvesting from low frequency vibrations *Research* **2019** 1087946

[9] Gao Z, Zhang X, Kulczyk-Malecka J, Chen Y, Bousser E, Kelly P and Xiao P 2021 Ceramic buckling for determining the residual stress in thin films *Scr. Mater.* **201** 113949

[10] Zanaty M, Fussinger T, Rogg A, Lovera A, Lambelet D, Vardi I, Wolfensberger T J, Baur C and Henein S 2019 Programmable multistable mechanisms for safe surgical puncturing *J. Med. Devices* **13** 021002

[11] Smreczak M, Tissot-Daguette L, Thalmann E, Baur C and Henein S 2022 A load cell with adjustable stiffness and zero offset tuning dedicated to electrical micro- and nanoprobing *Precis. Eng.* **76** 208–25

[12] Berntsen L, Gosenshuis D H and Herder J L 2014 Design of a compliant monolithic internally statically balanced four-bar mechanism *Proc. ASME 2014 Int. Design Engineering Technical Conf.s and Computers and Information in Engineering Conf. Volume 5A: 38th Mechanisms and Robotics Conf. (Buffalo, NY, USA)* p V05AT08A040

[13] Camescasse B, Fernandes A and Pouget J 2014 Bistable buckled beam and force actuation: experimental validations *Int. J. Solids Struct.* **51** 1750–7

[14] Cazottes P, Fernandes A, Pouget J and Hafez M 2009 Bistable buckled beam: modeling of actuating force and experimental validations *J. Mech. Des.* **131** 101001

[15] Zhao H, Han D, Zhang L and Bi S 2017 Design of a stiffness-adjustable compliant linear-motion mechanism *Precis. Eng.* **48** 305–14

[16] Wu Y and Lan C 2014 Linear variable-stiffness mechanisms based on preloaded curved beams *J. Mech. Des.* **136** 122302

[17] Barel M Y, Machekposhti D F, Herder J L, Tolou N and Sitti M 2018 Permanent preloading by acceleration for statically balancing mems devices *2018 Int. Conf. on Reconfigurable Mechanisms and Robots (Delft, Netherlands)* pp 1–11

[18] Qiu J, Lang J H and Slocum A H 2004 A curved-beam bistable mechanism *J. Microelectromech. Syst.* **13** 137–46

[19] Xu Q 2017 Design of a large-stroke bistable mechanism for the application in constant-force micropositioning stage *J. Mech. Robot.* **9** 011006

[20] Steiner H, Hortschitz W, Stifter M and Keplinger F 2014 Thermal actuated passive bistable MEMS switch *2014 Microelectronic Systems Symp. (Vienna, Austria)* pp 1–5

[21] Yang Y-J, Liao B-T and Kuo W-C 2007 A novel 2 × 2 MEMS optical switch using the split cross-bar design *J. Micromech. Microeng.* **17** 875

[22] Erbil S O, Hatipoglu U, Yanik C, Ghavami M, Ari A B, Yuksel M and Hanay M S 2020 Full electrostatic control of nanomechanical buckling *Phys. Rev. Lett.* **124** 046101

[23] de Laat M L C, Pérez Garza H H, Herder J L and Ghatkesar M K 2016 A review on *in situ* stiffness adjustment methods in MEMS *J. Micromech. Microeng.* **26** 063001

[24] Leplan H, Geenen B, Robic J Y and Pauleau Y 1995 Residual stresses in evaporated silicon dioxide thin films: correlation with deposition parameters and aging behavior *J. Appl. Phys.* **78** 962–8

[25] Yang J, Gaspar J and Paul O 2008 Fracture properties of LPCVD silicon nitride and thermally grown silicon oxide thin films from the load-deflection of long Si_3N_4 and SiO_2/Si3N_4 diaphragms *J. Microelectromech. Syst.* **17** 1120–34

[26] Laconte J, Iker F, Jorez S, André N, Proost J, Pardoen T, Flandre D and Raskin J-P 2004 Thin films stress extraction using micromachined structures and wafer curvature measurements *Microelectron. Eng.* **76** 219–26

[27] Tissot-Daguette L and Henein S 2024 *Flexure based mechanism with reduced stiffness* Patent EP24199124.9 applicant: EPFL

[28] Iqbal S, Malik A A and Shakoor R I 2019 Design and analysis of novel micro displacement amplification mechanism actuated by chevron shaped thermal actuators *Microsyst. Technol.* **25** 861–75

[29] Howell L L, McLain T W, Baker M S and Lott C D 2006 Techniques in the design of thermomechanical microactuators *MEMS/NEMS* ed C T Leondes (Springer)

[30] Que L, Park J-S and Gianchandani Y B 1999 Bent-beam electro-thermal actuators for high force applications *Technical Digest. IEEE Int. MEMS 99 Conf. 12th IEEE Int. Conf. on Micro Electro Mechanical Systems (Orlando, FL, USA)* pp 31–36

[31] Kommanaboina N M, Yallew T S, Bagolini A and Pantano M F 2024 A C-shaped hinge for displacement magnification in MEMS rotational structures *Microsyst. Nanoeng.* **10** 5

[32] Gianchandani Y B and Najafi K 1996 Bent-beam strain sensors *J. Microelectromech. Syst.* **5** 52–58

[33] Bagolini A, Margesin B, Faes A, Turco G and Giacomozzi F 2004 Novel test structures for stress diagnosis in micromechanics *Sens. Actuators* A **115** 494–500

[34] Mastropaolo E, Latif R, Grady E and Cheung R 2013 Control of stress in tantalum thin films for the fabrication of 3D MEMS structures *J. Vac. Sci. Technol.* B **31** 06FD02

[35] Elbrecht L, Storm U, Catanescu R and Binder J 1997 Comparison of stress measurement techniques in surface micromachining *J. Micromech. Microeng.* **7** 151

[36] Dijksman J F 1979 A study of some aspects of the mechanical behaviour of cross-spring pivots and plate spring mechanisms with negative stiffness *PhD Thesis* (TU Delft)

[37] Liang H, Hao G, Olszewski O Z and Pakrashi V 2022 Ultra-low wide bandwidth vibrational energy harvesting using a statically balanced compliant mechanism *Int. J. Mech. Sci.* **219** 107130

[38] Ma F and Chen G 2017 Bi-BCM: a closed-form solution for fixed-guided beams in compliant mechanisms *J. Mech. Robot.* **9** 014501

[39] Numić A, Blad T W A and van Keulen F 2021 Effect of matching buckling loads on post-buckling behavior in compliant mechanisms *Proc. ASME 2021 Int. Design Engineering Technical Conf. and Computers and Information in Engineering Conf. Volume 8A: 45th Mechanisms and Robotics Conf.* pp V08AT08A010

[40] Tissot-Daguette L, Schneegans H, Gubler Q, Baur C and Henein S 2022 Rectilinear translation four-bar flexure mechanism based on four remote center compliance pivots *Proc. 22nd Int. Conf. of the European Society for Precision Engineering and Nanotechnology* (*Geneva CH*) ICE22117

[41] Tan X, Wang B, Wang L, Zhu S, Chen S, Yao K and Xu P 2022 Effect of beam configuration on its multistable and negative stiffness properties *Compos. Struct.* **286** 115308
[42] Henein S 2000 Conception des structures articulées à guidages flexibles de haute précision *PhD Thesis (EPFL)*
[43] Tissot-Daguette L, Schneegans H, Thalmann E and Henein S 2022 Analytical modeling and experimental validation of rotationally actuated pinned–pinned and fixed–pinned buckled beam bistable mechanisms *Mech. Mach. Theory* **174** 104874
[44] Kobeda E and Irene E A 1986 A measurement of intrinsic SiO_2 film stress resulting from low temperature thermal oxidation of Si *J. Vac. Sci. Technol.* B **4** 720–2
[45] Hopcroft M A, Nix W D and Kenny T W 2010 What is the Young's modulus of silicon? *J. Microelectromech. Syst.* **19** 229–38
[46] Zhao J, Jia J, He X and Wang H 2008 Post-buckling and snap-through behavior of inclined slender beams *J. Appl. Mech.* **75** 041020
[47] Thalmann E 2020. Flexure pivot oscillators for mechanical watches *PhD Thesis (EPFL)*
[48] Despont M, Palmieri M, Dubochet O and Petremand Y 2020. *Elastic element for a micromechanical system* Patent CH718081B1 applicant: CSEM
[49] Tissot-Daguette L, Prêcheur Llarena S, Baur C and Henein S 2024 Fully compliant snap-through bistable gripper mechanism based on a pinned-pinned buckled beam *Proc. 24nd Int. Conf. of the European Society for Precision Engineering and Nanotechnology Dublin, Ire* (ICE24230)
[50] Thalmann E and Henein S 2022 Triple crossed flexure pivot based on a zero parasitic center shift kinematic design *J. Mech. Robot.* **14** 045001
[51] Tissot-Daguette L, Cosandier F, Thalmann E and Henein S 2024 Near-zero parasitic shift flexure pivots based on coupled n-RRR planar parallel mechanisms *J. Mech. Robot.* **16** 111006
[52] Howell L L 2001 *Compliant Mechanism* (Wiley)
[53] Hopkins J 2013 Synthesis through freedom and constraint topologies *Handbook of Compliant Mechanisms* ed L L Howell, S P Magleby and B M Olsen (Wiley)
[54] Vangbo M 1998 An analytical analysis of a compressed bistable buckled beam *Sens. Actuators* A **69** 212–6
[55] Camescasse B, Fernandes A and Pouget J 2013 Bistable buckled beam: Elastica modeling and analysis of static actuation *Int. J. Solids Struct.* **50** 2881–93
[56] Hussein H, Wang C, Esteves R A, Kraft M and Fariborzi H 2024 Near-zero stiffness accelerometer with buckling of tunable electrothermal microbeams *Microsyst. Nanoeng.* **10** 43
[57] Inaudi D, Blin R, Timotijevic B, Zaman Bayat D, Petremand Y, Luetzelschwab M and Niketic N 2019 Integrated optics inclinometers for SHM international conference on smart monitoring *Assessment and Rehabilitation of Civil Structures Potsdam, DE* (available at: https://smartec.ch)
[58] Gasparin E, Hoogerwerf A, Bayat D, Spinola Durante G, Petremand Y, Tormen M, Despont M and Close G 2024 An integrated MEMS magnetic gradiometer rejecting vibrations and stray fields *2024 IEEE European Solid-State Electronics Research Conf. (ESSERC)* (*Bruges, BEL*) pp 532–5
[59] Sun R, Chen X and Liu Y 2023 Ultra-low frequency vibration energy harvesting: mechanisms, enhancement techniques, and scaling laws *Energy Convers. Manage.* **276** 116585
[60] Schneegans H, Thalmann E and Henein S 2021 Shaking force balancing of a 2-DOF isotropic horological oscillator *Precis. Eng.* **74** 294–303